A&A 668, A169 (2022)
https://doi.org/10.1051/0004-6361/202244522

Astronomy & Astrophysics

Ion irradiation triggers the formation of the precursors of complex organics in space

The case of formaldehyde and acetaldehyde

R. G. Urso[1,2], E. Hénault[3], R. Brunetto[3], D. Baklouti[3], G. A. Baratta[2], Z. Djouadi[3], A. Elsaesser[1], C. Scirè[2], G. Strazzulla[2], and M. E. Palumbo[2]

[1] Experimental Biophysics and Space Sciences, Institute of Experimental Physics, Freie Universitaet, Arnimallee 14, 14195 Berlin, Germany
e-mail: riccardo.urso@inaf.it
[2] INAF–Osservatorio Astrofisico di Catania, via Santa Sofia 78, 95123 Catania, Italy
[3] Université Paris-Saclay, CNRS, Institut d'Astrophysique Spatiale, 91405 Orsay, France

Received 16 July 2022 / Accepted 19 October 2022

ABSTRACT

Context. Cosmic rays and solar energetic particles induce changes in the composition of compounds frozen onto dust grains in the interstellar medium (ISM), in comets, and on the surfaces of atmosphere-less small bodies in the outer Solar System. This induces the destruction of pristine compounds and triggers the formation of various species, including the precursors of complex organics.
Aims. We investigate the role of energetic ions in the formation of formaldehyde (H_2CO) and acetaldehyde (CH_3CHO), which are observed in the ISM and in comets, and which are thought to be the precursors of more complex compounds such as hexamethylenetetramine (HMT), which is found in carbonaceous chondrites and in laboratory samples produced after the irradiation and warm-up of astrophysical ices.
Methods. We performed ion irradiation of water, methanol, and ammonia mixtures at 14–18 K. We bombarded frozen films with 40–200 keV H^+ that simulate solar energetic particles and low-energy cosmic rays. Samples were analysed by infrared transmission spectroscopy.
Results. Among other molecules, we observe the formation of H_2CO and CH_3CHO, and we find that their abundance depends on the dose and on the stoichiometry of the mixtures. We find that the H_2CO abundance reaches the highest value after a dose of 10 eV/16u and then it decreases as the dose increases.
Conclusions. The data suggest that surfaces exposed to high doses are depleted in H_2CO. This explains why the amount of HMT in organic residues and that formed after irradiation of ices depends on the dose deposited in the ice. Because the H_2CO abundance decreases at doses higher than 10 eV/16u, a lower quantity of H_2CO is available to form HMT during the subsequent warm-up. The H_2CO abundances caused by ion bombardment are insufficient to explain the ISM abundances, but ion bombardment can account for the abundance of CH_3CHO towards the ISM and comets.

Key words. astrochemistry – ISM: molecules – ISM: abundances – methods: laboratory: solid state – techniques: spectroscopic

1. Introduction

Frozen compounds are present on dust grains in the interstellar medium (ISM; e.g. Boogert et al. 2015) and on the surface of small bodies in the Solar System, such as comets (e.g. Bockelée-Morvan et al. 2000; Altwegg et al. 2017), satellites of giant planets (e.g. Johnson 2005; Spencer & Nimmo 2013; Dougherty & Spilker 2018), Kuiper-belt (KBOs), and trans-neptunian objects (TNOs; e.g. Cruikshank et al. 1998; Brown et al. 2011; Grundy et al. 2020; Barucci & Merlin 2020). Various KBOs and TNOs exhibit frozen compounds together with red slopes in the visible and near-infrared (NIR) spectra that could be attributed to complex C-rich materials (Brunetto et al. 2006; Brown et al. 2011; Dalle Ore et al. 2011). Complex organics are also found in materials sampled from asteroids (e.g. Chan et al. 2021; Pilorget et al. 2021; Parker et al. 2022), in interplanetary dust particles (IDPs; e.g. Chan et al. 2020) and carbonaceous chondrites (CC; e.g. Sephton 2002; Busemann et al. 2006; Schmitt-Kopplin et al. 2010; Oba et al. 2020, 2022).

Laboratory experiments allow us to shed light on the physical and chemical properties of small bodies and to improve our understanding of the processes that contribute to the formation of complex organics. Experiments allowed studying how energetically charged particles in space, such as cosmic rays (CR) and solar particles, affect the spectral properties of frozen surfaces in the ISM and in the Solar System, such as the appearance of red slopes in irradiated ices (e.g. Strazzulla et al. 1983; Moore et al. 1996; Brunetto et al. 2006; Palumbo 2006; Dartois et al. 2015; Rothard et al. 2017; Poston et al. 2018). Changes primarily depend on the initial composition of the ice, the source of processing, and the irradiation dose (e.g. Rothard et al. 2017). Simple and complex compounds are formed after irradiation of mixtures that simulate the pristine composition of astrophysical ices (e.g. Moore et al. 1996; Palumbo et al. 1997; Kaňuchová et al. 2016; Urso et al. 2019). Among them, vibrational mode bands attributed to aldehydes are found in the mid-IR spectra of samples exposed to UV photons and ion irradiation. In particular, formaldehyde (H_2CO) and acetaldehyde (CH_3CHO) have been reported among the byproducts of irradiation of frozen mixtures containing H-, C-, and O-bearing compounds (e.g. Khare et al. 1989; Moore & Hudson 1998; Palumbo et al. 1999). In space, solid-phase H_2CO is likely identified toward massive

young stellar objects (MYSOs) and low-mass YSOs (LYSOs), with abundances of 0.06–6.00 relative to CH_3OH (Bottinelli et al. 2007; Boogert et al. 2015). In the Solar System, H_2CO is detected in comets (e.g. Mitchell et al. 1987; Altwegg et al. 2019) with abundances that span between 0.02 and 5 with respect to CH_3OH (e.g. le Roy et al. 2015; Boogert et al. 2015; Schuhmann et al. 2019). Solid-phase CH_3CHO is only tentatively detected in the ISM and in comets, while it is observed in the gas-phase in both environments (e.g. Cazaux et al. 2003; Crovisier et al. 2004; Öberg et al. 2010; Jaber et al. 2014; Codella et al. 2015; Schuhmann et al. 2019). Information on solid-phase CH_3CHO is lacking, possibly because its main vibrational mode bands overlap with those of other species. In particular, $HCOO^-$ shows a vibrational feature at the same wavelength and can contribute to the 1350 cm^{-1} feature (e.g. Schutte et al. 1999).

In space, aldehydes are among the frozen compounds that can react to form more complex species. Reactions are also favoured by thermal processing that increases the diffusion and reactivity of molecules (e.g. Mispelaer et al. 2013; Theulé et al. 2013; Vinogradoff et al. 2013). When irradiation and thermal processing of astrophysical ices is simulated in the laboratory, a complex organic refractory material forms. Organic refractory residues are laboratory analogues of cometary refractory organics (e.g. Strazzulla & Johnson 1991; Baratta et al. 2019), of the organics in extraterrestral samples (e.g. Nuevo et al. 2008; de Marcellus et al. 2017), and of organic materials that can form on the surface of KBOs and TNOs (e.g. Strazzulla et al. 2003; Urso et al. 2020b). The characterization of residues reveals various astrobiologically relevant compounds, including amino acids, nucleobases, and sugars (Danger et al. 2013; Fresneau et al. 2017; Meinert et al. 2016; Nuevo et al. 2018; Urso et al. 2020b). According to Vinogradoff et al. (2012b), together with NH_3 and HCOOH, which act as a catalyst, H_2CO is one of the precursor of hexamethylenetetramine (HMT). This is one of the most abundant organics detected in residues and forms at relatively high temperatures (>280 K) during the warm-up of ices. HMT was recently found in the carbonaceous chondrites Murchison, Murray, and Tagish Lake (Oba et al. 2020), and in the laboratory, it forms after UV and ion irradiation at 10–20 K and subsequent warm-up to room temperature of mixtures containing water (H_2O), methanol (CH_3OH), and ammonia (NH_3, Hulett et al. 1971; Bernstein et al. 1995; Cottin et al. 2001; Vinogradoff et al. 2013; Danger et al. 2016; Urso et al. 2020b). Urso et al. (2020b) reported that the composition of organic refractory residues depends on the extent of irradiation experienced by ices. They also found that the HMT abundance decreased when the dose was increased.

CH_3CHO is also invoked as a precursor of various complex compounds. Laboratory experiments that simulated the thermal processing of CH_3CHO-rich ices showed that CH_3CHO reacts with NH_3 to form α-aminoethanol ($NH_2CH(CH_3)OH$) above 100 K (Duvernay et al. 2010). Furthermore, above 70 K and in presence of HCOOH, the reaction between CH_3CHO and NH_3 leads to the CH_3CHO-NH_3 trimer after the formation of the reaction intermediates α-aminoethanol and ethanimine (Vinogradoff et al. 2012a).

We here report new experiments that we performed to investigate the role of ion irradiation in the production of H_2CO and CH_3CHO. We study how their abundance is affected by the dose and we discuss how the formation of HMT can be affected by the destruction of H_2CO, its precursor. For this study, we deposited H_2O:CH_3OH:NH_3 mixtures at 14–18 K and exposed them to 40 and 200 keV H^+. H_2O, CH_3OH, and NH_3 mixtures were chosen because they are among the most abundant solid-phase compounds observed in YSOs (e.g. Caselli & Ceccarelli 2012; Boogert et al. 2015) and in small bodies in the outer Solar System (e.g. Cruikshank et al. 1998; Delsanti et al. 2010; Grundy et al. 2016; Barucci & Merlin 2020). Furthermore, organic refractory residues produced after irradiation of H_2O:CH_3OH:NH_3 mixtures are well characterized and show complex organics, including HMT (e.g. Bernstein et al. 1995; Danger et al. 2016; Urso et al. 2020b). We can thus interpret our results by taking into account similar experiments reported in literature. The irradiation with 40 and 200 keV H^+ allows us to simulate the effects of solar charged particles and CR on icy surfaces in the Solar System and on icy grain mantles. As discussed by Mewaldt et al. (2007) and Urso et al. (2020a), protons in the range of tens of keV are abundant in the spectrum of solar energetic particles (SEP) impinging on frozen surfaces in the outer Solar System. Furthermore, several previous studies used hundreds ok keV H^+ to simulate the effects of low-energy CR (e.g. Palumbo 2006; Islam et al. 2014; Urso et al. 2019).

2. Experimental methods

The ion irradiation experiments were performed at the Intitut d'Astrophysique Spatiale, Irène Joliot-Curie Laboratoire (IAS-IJCLab Orsay, France) and at the Laboratory of Experimental Astrophysics (LASp) at the Istituto Nazionale di Astrofisica INAF-Osservatorio Astrofisico di Catania (Catania, Italy). We used the IrradiatioN de Glaces et Météorites Analysées par Réflectance VIS-IR (INGMAR) setup at IAS-IJCLab to irradiate ices with 40 keV H^+ by means of the SIDONIE accelerator (Chauvin et al. 2004). The setup at the LASp allows accelerating ions up to 200–400 keV (Fulvio et al. 2009; Urso et al. 2016). For this work, we used 200 keV H^+. Although the two experimental setups show distinct characteristics, they both consist of high vacuum chambers ($P \sim 10^{-8}$–10^{-9} mbar), where He cryocoolers allow cooling substrates down to ~15 K. H_2O:CH_3OH:NH_3 gaseous mixtures were injected in the vacuum chambers, where they condensed on the cold substrates. The resulting frozen films were then exposed to H^+ beams that were rastered on samples, in order to ensure a homogeneous covering of their surfaces.

The energy of impinging ions determines their penetration depth in the frozen mixture. According to simulations performed with the SRIM software (Ziegler et al. 2008), 40 keV and 200 keV H^+ implant in H_2O:CH_3OH:NH_3 mixtures within 1 μm and 3.3 μm, respectively. We therefore deposited frozen films with thicknesses that were lower than the H^+ implantation depth to ensure that the impinging particles released their energy homogeneously within the ice, and to limit their implantation. In particular, for the experiments with 40 keV H^+, we deposited films between 0.4 and 0.6 μm, while in the case of irradiation with 200 keV, we deposited 0.5 and 1.2 μm thick films. During ion irradiation, we integrated the ion current to estimate the fluence, that is, the number of impinging ions cm^{-2}. We then estimated the dose, that is, the energy deposited per molecule in the sample by incident particles, by multiplying the fluence by the stopping power (eV cm^2/16u) calculated with SRIM. We give the dose in eV/16u, where 16u is the atomic mass unit of a CH_4 molecule that we take as a reference (Strazzulla & Johnson 1991).

To properly simulate the ion irradiation of frozen surfaces, we kept the ion current in the range of some hundred nA and below 1 μA. For an ion current density of 1 μA cm^{-2}, the flux is equal to 6.25×10^{12} ions cm^{-2} s^{-1}. This value prevents the macroscopic heating of the samples. Furthermore, the low current is required to ensure that enough time passes between

Table 1. List of all the experiments. Frozen mixtures are deposited and irradiated at 14–18 K.

Experiment label	H_2O:CH_3OH:NH_3 mixture ratio	H^+ energy (keV)	Dose min. (eV/16u)	Dose max. (eV/16u)
3_200_L	3:1:1	200	2	23
3_200_H	3:1:1	200	16	80
1_200_L	1:1:1	200	2	27
1_200_H	1:1:1	200	19	93
3_40	3:1:1	40	7	54
1_40	1:1:1	40	26	103

Notes. Experiments are labelled as follows: the first number gives the amount of H_2O with respect to CH_3OH and NH_3 in the mixture; the second number gives the energy of the H^+ beam used for irradiation. For replicate experiments, the last letter represents the range of dose used; L: low dose; H: high dose.

the arrival of two ions on the same target area. Ions travelling through the target cause ionizations and excitations of molecules and the formation of molecular fragments and radicals, whose recombination forms species that were not present in the original sample (e.g. Rothard et al. 2017). The whole process, from the excitation to the recombination and thus relaxation, requires about 10^{-12} s or less. The mixtures we deposited at 14–18 K had a density of about 0.9 g cm^{-3}. In these samples, keV protons create a radial struggle of $r = 1.7\times10^{-5}$ cm as calculated by means of the SRIM software. The ion track within the ice can be approximated to a cylinder with a section area $a = \pi r^2$, equal to 9.1×10^{-10} cm^2, which we can approximate to 10^{-9} cm^2. Thus, it is necessary to reach a fluence of 10^9 ions cm^{-2} to fully cover the surface of a sample of 1 cm^2. Taking into account a constant flux value as that used in our experiment, i.e. about 6.25×10^{12} ions cm^{-2} s^{-1}, a fluence of 10^9 ions cm^{-2} is reached after 1.6×10^{-2} s. This is the time required for an impinging ion to hit the same target area a already excited by a former ion in our experiments. This time is about 10^{10} times longer than the relaxation time along the ion track (about 10^{-12} s). As a consequence, impinging ions always travel through volumes of ices that are stable and relaxed. This allows our laboratory experiments to be representative of the particle irradiation taking place in astrophysical ices exposed to cosmic and solar charged particles.

Samples are analysed in situ by means of transmission Fourier-Transform infrared spectroscopy (FT-IR) with a resolution of 1 cm^{-1}. In the INGMAR setup, the IR beam arrives on the sample with an angle of 10° with respect to the surface normal, while at LASp the IR beam arrives with an incident angle of 45° with respect to the surface normal.

H_2O, CH_3OH, and NH_3 are deposited at 14–18 K on IR-transparent substrates (ZnSe or KBr) and bombarded with 40 and 200 keV H^+. Spectra are acquired after the deposition and after each irradiation step, in order to monitor the sample spectral evolution as a function of irradiation dose. Spectra are then analysed to obtain qualitative and quantitative estimations on the newly-formed compounds. We give the abundance of the newly-formed compounds $N(X)$ by estimating the column density, i.e. $N(X) = \frac{\int \tau(\nu)\mathrm{d}\nu}{A}$, where $\tau(\nu)$ is the optical depth (–ln T, transmittance) and A is the band strength (cm molecule^{-1}) of the vibrational mode band taken into account.

The comparison between experimental results obtained in different laboratories is not trivial. We thus carefully plan experiments and we use the same procedures to acquire, reduce, and analyse data so to minimise the differences that arise when comparing different experiments. This allow us to obtain qualitative and quantitative information that show consistent trends, thus confirming the reliability of our results.

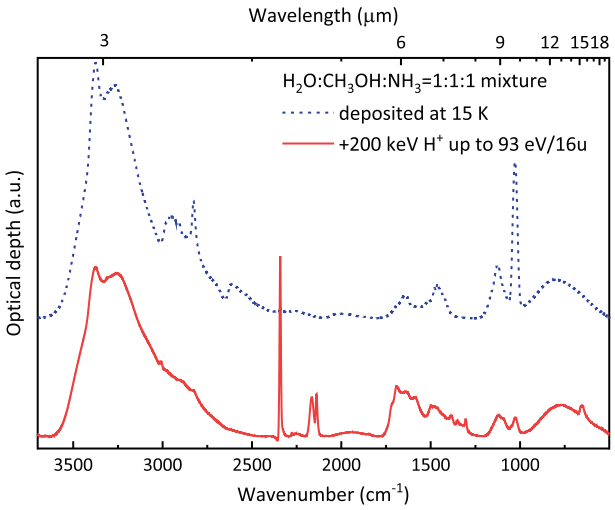

Fig. 1. Mid-IR spectra of a H_2O:CH_3OH:NH_3 = 1:1:1 mixture as deposited (dashed blue line) and after irradiation with 200 keV H^+ (solid red line). Bottom axis: wavenumber (cm^{-1}). Top axis: wavelength (μm). Spectra are on the same optical depth scale with an offset to avoid superposition.

3. Results

Table 1 groups all the experiments taken into account in this work. Experiments are labelled according to (i) the amount of H_2O with respect to CH_3OH and NH_3 in the mixture and (ii) the energy of the H^+ beam used to bombard the samples. In the case of the experiments performed with 200 keV H^+, we deposit the same mixture ratio twice, in the same experimental conditions, and we perform irradiation in two ranges of dose that overlap with each other. These experiments are labelled according to the dose range we investigate (*L* for the low dose range and *H* for the high dose range).

3.1. Methanol destruction and methane formation

Figure 1 shows the spectra of a H_2O:CH_3OH:NH_3 = 1:1:1 mixture before and after irradiation with 200 keV H^+. Before irradiation we observe the N-H stretching mode band of NH_3 at 3375 cm^{-1}, the O-H stretching mode band in water and CH_3OH at about 3270 cm^{-1}, the C-H stretching mode bands of CH_3OH

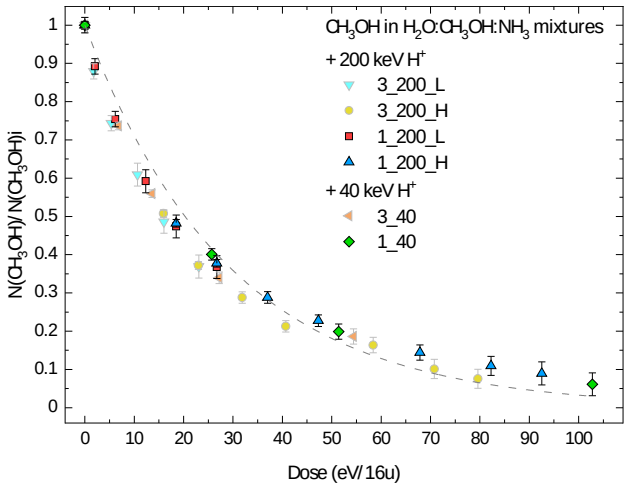

Fig. 2. Column density of CH_3OH during irradiation with 40–200 keV H^+ in H_2O:CH_3OH:NH_3 normalized to the initial amount of methanol, $(CH_3OH)i$. The CH_3OH column density is estimated from the analysis of the 1025 cm^{-1} band. Experimental data are fitted with an exponential curve $y = e^{-\sigma D}$ (dashed grey line).

between about 2980 and 2830 cm^{-1}, two broad features between 1720 and 1370 cm^{-1} attributed to bending modes in water and NH_3 molecules, a feature at 1125 attributed to the wagging mode in NH_3 and to the rocking mode in CH_3OH, the C-O stretching mode of CH_3OH at 1025 cm^{-1}, and the water libration mode band between about 990 and 500 cm^{-1} (e.g. Urso et al. 2020b). Irradiation determines evident changes in the spectra. The features at about 3300 and 1025 cm^{-1} decrease and new bands appear. In particular, the CH_3OH band at 1025 cm^{-1} decreases with increasing dose, following an exponential decay, because of the ion-induced destruction of CH_3OH. Figure 2 shows the variation in the CH_3OH abundance as a function of the dose. We fit the data with an exponential curve (Eq. (1)),

$$y = e^{-\sigma D}, \quad (1)$$

where σ is the cross section, which is found to be 0.34 16u/eV, and D is the dose in eV/16u. About 50% of CH_3OH is destroyed after a dose of about 20 eV/16u, and only 10% of CH_3OH is left at about 70 eV/16u. The analysis also shows that about 3% of methanol survives the highest irradiation dose. The most intense new features are those attributed to CO_2 (2345 cm^{-1}), OCN^- (2165 cm^{-1}), and CO (2139 cm^{-1}). Furthermore, Fig. 3 shows a zoom in the 1600–1200 cm^{-1} range before (panel A) and after irradiation with 40 and 200 keV H^+ (panel B). In this range, several new features appear after irradiation. The band centred at 1305 cm^{-1} is attributed to CH_4 that formed after irradiation. Figure 4 shows the CH_4 abundance as a function of irradiation dose. For our estimations, we used the CH_4 1300 cm^{-1} band strength given by Mulas et al. (1998). The highest column density (4.6%) is reached after about 50 eV/16u. Figure 4 also shows the CH_4 formation σ that we estimate by means of Eq. (2),

$$y = y_\infty(1 - e^{-\sigma D}), \quad (2)$$

where y_∞ is the asymptotic value of the $N(CH_4)/N(CH_3OH)_i$ ratio. Table 2 reports the values of y_∞ and σ for each experiment. The analysis of the CH_3OH destruction and of the CH_4 formation does not show differences attributable to the H^+ energy used to irradiate samples.

Table 2. CH_4 formation cross section in H_2O:CH_3OH:NH_3 mixtures after H^+ bombardment.

Experiment	σ (16u/eV)	y_∞
3_200_L	0.035 ± 0.011	0.045 ± 0.009
3_200_H	0.048 ± 0.005	0.042 ±0.001
1_200_L	0.053 ± 0.004	0.037 ± 0.002
1_200_H	0.036 ± 0.001	0.048 ± 0.001
3_40	0.051 ± 0.005	0.035 ± 0.0014
1_40	0.043 ± 0.006	0.046 ± 0.002

Notes. Data from the analysis of the 1305 cm^{-1} band.

3.2. Formaldehyde and acetaldehyde formation

Various vibrational mode bands attributed to H_2CO (1720, 1500, 1250 cm^{-1}) and CH_3CHO (1720, 1382, 1350 cm^{-1}, e.g. Moore & Hudson 1998; Urso et al. 2020b) are found in both 3:1:1 and 1:1:1 mixtures after irradiation. We perform quantitative analysis to study the evolution of their abundance with increasing irradiation dose. For the analysis, we do not consider the 1720 cm^{-1} band as it contains contributions from all the –C=O bearing species in the samples. Furthermore, cautions has to be taken because of other features in the same spectral range (NH_2CHO at 1385 cm^{-1}, NH_4^+ at 1480 and 1460 cm^{-1}, $HCOO^-$ at 1385 and 1350 cm^{-1}; e.g. Brucato et al. 2006; Raunier et al. 2004; Schutte et al. 1999).

H_2CO column densities were estimated by analysing the CH_2 rocking mode band at 1250 cm^{-1} using the band strength value given by Bouilloud et al. (2015), that is, 1.5×10^{-18} cm molecule^{-1}. Panel A of Fig. 5 shows the H_2CO abundance with respect to the initial abundance of CH_3OH as a function of the dose. In all the experiments, the H_2CO abundance increases rapidly at low doses and the highest abundance is observed at about 10 eV/16u. At this dose, the irradiation of 3:1:1 mixtures produces 6.2% of H_2CO, and the irradiation of 1:1:1 mixtures produces 2.4%. At higher irradiation doses the H_2CO abundance starts to decrease, following an exponential decay. At about 30 eV/16u, the 1:1:1 and 3:1:1 mixtures show comparable amounts of H_2CO. At the highest irradiation dose we investigated, the H_2CO band is at the detection limit and the abundance is about 1% with respect to the initial amount of CH_3OH. In Fig. 5 we also show the abundance of H_2CO with respect to the amount of CH_3OH at the same dose. Again, the ratio increases at low doses, with higher abundances in the case of the 3:1:1 mixtures. At doses higher than 50 eV/16u both H_2CO and CH_3OH are efficiently destroyed and the observed trend is based on features that are at the detection limits.

We estimated the CH_3CHO abundance by analysing the 1350 cm^{-1} band. Various features overlap with this band, in particular the νC-O of $HCOO^-$ (Schutte et al. 1999). We therefore also analysed the 1580 cm^{-1} band, which is attributed to $HCOO^-$ alone (Schutte et al. 1999), and we calculated the 1580/1350 band area ratio in our experiments and in the spectrum of a H_2CO:NH_3:HCOOH mixture reported by Vinogradoff et al. (2011), in order to check the relative intensity of the two bands and to verify that the 1350 cm^{-1} band is not mainly due to $HCOO^-$. Vinogradoff et al. (2011) attributed both bands to $HCOO^-$ because their mixtures did not contain CH_3CHO. When we use their 1580/1350 ratio as a reference, we would find a similar 1580/1350 band ratio if our mixtures were also to contain manly $HCOO^-$. However, our mixtures show averages of the

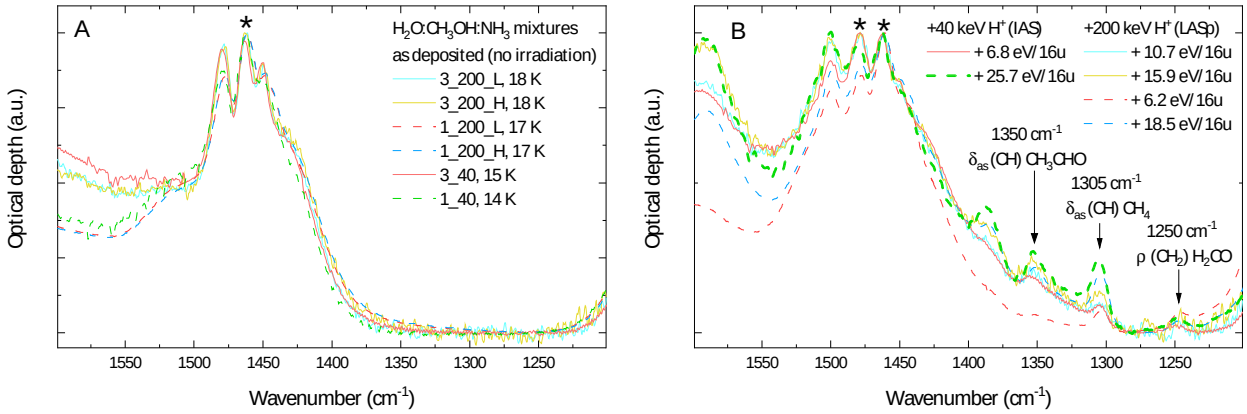

Fig. 3. 1600–1200 cm^{-1} spectra of H_2O:CH_3OH:NH_3 mixtures as deposited (*panel A*) and after irradiation with 40 or 200 keV H^+. For a better comparison, spectra were normalized to the most intense peak (marked with an asterisk) between 1478 and 1462 cm^{-1}. In the spectra in *panel A* the spectral continuum at about 1550 cm^{-1} is affected by the amount of water in the mixture. The continuum is higher in 3:1:1 mixtures because of the higher amount of water with respect to 1:1:1 mixtures.

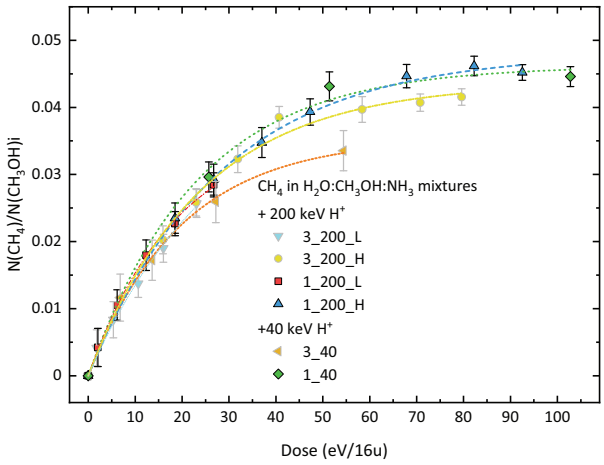

Fig. 4. CH_4 abundance relative to the initial amount of methanol, $(CH_3OH)i$ with increasing irradiation dose. The CH_4 column density is estimated from the analysis of the 1305 cm^{-1} band; the CH_3OH column density is estimated from the 1025 cm^{-1} band.

Table 3. CH_3CHO formation cross section in H_2O:CH_3OH:NH_3 mixtures after ion bombardment.

Experiment	σ (16u/eV) [gauss] (linear)	y_∞ [gauss] (linear)
3_200_L , 3_200_H	[0.037] (0.038)	[0.104] (0.041)
1_200_L , 1_200_H	[0.061] (0.060)	[0.040] (0.022)
3_40	[0.055] (0.052)	[0.115] (0.044)
1_40	[0.055] (0.058)	[0.051] (0.026)

Notes. [gauss] refer to cross section and asymptotic values estimated from the analysis of the 1350 cm^{-1} band area through gaussian fit; (linear) refers to cross section and asymptotic values estimated from the analysis of the 1350 cm^{-1} band area after the subtraction of the linear continuum below the band (see Fig. B.2).

1580/1350 band ratios that are as low as about 50% of the ratio in Vinogradoff et al. (2011). This preliminary analysis gives us confidence in attributing the 1350 cm^{-1} band to CH_3CHO, although dedicated studies with more sensitive techniques are needed to estimate the relative amounts of $HCOO^-$ and CH_3CHO in irradiated mixtures, such as in situ mass spectrometry currently under implementation at LASp.

For our estimations of the CH_3CHO abundance, we took into account a 1350 cm^{-1} band strength of 7.11×10^{-18} cm molecule^{-1} (Hudson & Ferrante 2020). This value is higher than the one given by Schutte et al. (1999), that is, 1.5×10^{-18} cm molecule^{-1}, and thus allows a more conservative estimation of the CH_3CHO abundance. We used two methods to estimate the 1350 cm^{-1} band area, as shown in Fig. B.2. We first subtracted a linear continuum between 1330 and 1360 cm^{-1} and then integrated the band intensity (Fig. B.2, panel A). This method tends to underestimate the band area because a relevant portion of it is found beneath the linear baseline that is subtracted to exclude other components. Panel A of Fig. 6 shows the results of the estimations. As in the case of H_2CO, the irradiation of more diluted mixtures results in a higher abundance of CH_3CHO. The irradiation of 3:1:1 mixtures up to 50 eV/16u determines the production of about the 4% of CH_3CHO. In 1:1:1 mixtures, the highest abundance is about 3%. We also performed multi-Gaussian fits between 1500 and 1300 cm^{-1} by simulating a Gaussian curve to fit the 1350 cm^{-1} band (Fig. B.2, panel B). This method estimates the total area of the 1350 cm^{-1} band from the baseline at optical depth zero. The estimated of the CH_3CHO abundances we obtained through the multi-Gaussian fits are reported in Fig. 6, panel B. CH_3CHO abundances reach 12% in 3:1:1 mixtures and 6% in 1:1:1 mixtures. We fitted the data in Fig. 6 with Eq. (2) to obtain the cross sections that are given in Table 3. The values of y_∞ vary according to the method we used to estimate the 1350 cm^{-1} band area. Figure 6, panel C, shows the ratio of the CH_3CHO abundance and the CH_3OH abundance at the same dose. The exponential trend of the data has to be attributed to the formation of CH_3CHO and the destruction of CH_3OH.

4. Discussion

The reactions induced by ion irradiation in ices are due to the transfer of kinetic energy between ions and the target molecules, resulting in their excitation and ionization along the ion track (e.g. Rothard et al. 2017). Figure B.1 shows that for both 40 and 200 keV H^+, the interaction occurs mainly through inelastic collisions between the impinging keV H^+ and the electronic cloud of the target molecules, while the contribution from elastic collisions, that is, the nuclear stopping power S_n, can be neglected. The similar values of inelastic stopping power of

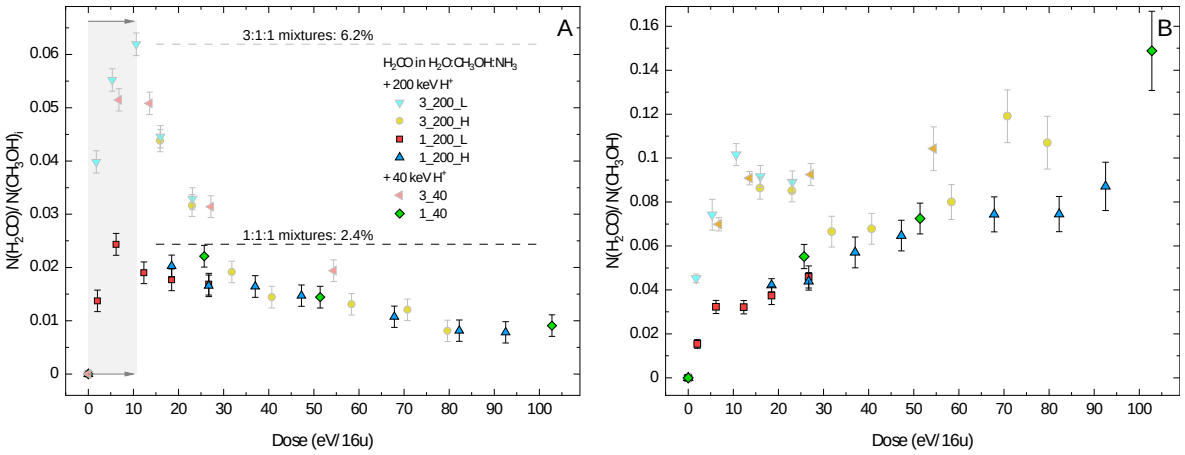

Fig. 5. H_2CO in H_2O:CH_3OH:NH_3 mixtures exposed to ion bombardment. Estimates are based on the analysis of the 1250 cm^{-1} band for H_2CO and 1025 cm^{-1} for CH_3OH and are normalized to the initial methanol abundance, $(CH_3OH)i$. Panel A: H_2CO as a function of dose, with respect to the amount of deposited CH_3OH. The grey area shows the range in which the H_2CO abundance was found to increase with increasing the dose. The horizontal dashed line indicates the maximum amount of H_2CO found in 1:1:1 mixtures (dashed black line) and 3:1:1 mixtures (dashed grey line). Panel B: H_2CO with respect to the CH_3OH at the same irradiation dose.

40 and 200 keV H^+ could explain the consistent results we obtain in all the experiments, with changes that can accordingly be attributed to the irradiation dose. However, the H^+ energy determines the H^+ penetration depth before their implantation in the ice (e.g. Urso et al. 2020a). The higher the H^+ energy, the higher the penetration depth.

4.1. Chemical changes induced by ion bombardment

The irradiation of H_2O:CH_3OH:NH_3 mixtures at 14–18 K determines the formation of CH_4 (Fig. 4), a compound observed in various star-forming regions and on frozen surfaces in the outer Solar System. The quantitative analyses show that cross sections and asymptotic values reported in Table 2 are comparable to those reported in literature (Islam et al. 2014). The CH_4 abundance reaches a plateau above 50 eV/16u, and at these doses, we find 4.5% of CH_4 with respect to the initial CH_3OH. This abundance represents the highest amount of CH_4 that can form on a CH_3OH-rich body exposed to irradiation. However, other processes could contribute to form CH_4 and thus increase its abundance with respect to CH_3OH. In the ISM, hydrogenation of C atoms on the dust grains forms CH_4 (e.g. Allen & Robinson 1977). On frozen small bodies, higher CH_4 abundances could be attributed to the accretion of pristine CH_4 from the presolar cloud, during the bodies formation, to the irradiation of other CH_4 precursors, or to the more efficient migration of CH_4 towards the surface as it is more volatile than CH_3OH (e.g. Fray & Schmitt 2009).

We also detect H_2CO and CH_3CHO. The highest amount of H_2CO with respect to CH_3OH, that is, 6%, is observed after irradiation of 3:1:1 mixtures up to about 10 eV/16u, while only 2% of H_2CO is found in 1:1:1 mixtures. In all mixtures, the H_2CO abundance decreases at doses higher than 10 eV/16u, revealing that ices exposed to a higher extent of irradiation will be depleted in H_2CO. Taking into account the most conservative approach, we find up to 4% of CH_3CHO with respect to the initial CH_3OH abundance. The CH_3CHO abundance could be as high as 12% by considering the data obtained through the multi-Gaussian fit of the 1350 cm^{-1} band. In Fig. 7 we show the ratio of the two aldehydes, H_2CO/CH_3CHO as a function of the dose. Ices exposed to a low extent of irradiation show a high ratio because of the efficient formation of H_2CO at low dose. At higher dose, the ratio decreases because H_2CO is destroyed, while the amount of CH_3CHO reaches a plateau. In our experiments, the formation of H_2CO could be explained by taking the dehydrogenation of CH_3OH induced by the impinging H^+ into account, in a mechanism similar to that of secondary electrons in CH_3OH-rich mixtures (Ciaravella et al. 2010). CH_3CHO could be formed through the reaction path reported by Bennett et al. (2005), which involves solid-phase CO and CH_4, which are both abundant byproducts of CH_3OH irradiation. The cleavage of a C-H bond in CH_4 would form CH_3 and a suprathermal H that would then react with CO, forming the formyl radical HCO. Neighbouring CH_3 and HCO would then recombine to form CH_3CHO. This mechanism involving CH_4 also explains why more quantities of CH_3CHO form during irradiation, as the CH_4 abundance also increases with the dose. We also find that both H_2CO and CH_3CHO are formed more efficiently in mixtures richer in H_2O. Although dedicated studies are needed to explain the role of H_2O in the production of aldehydes, it is possible that on one hand, the aldehyde formation is independent of the abundance of H_2O and during irradiation aldehydes would destroy more efficiently simply because they are more highly concentrated in the samples; on the other hand, H_2O could take part in the reactions leading to aldehydes, favouring their formation through a reaction network that includes OH radicals and H.

Aldehydes are invoked as precursors of complex organics that can form in ices exposed to ion irradiation and thermal processing in space. In particular, H_2CO is a precursor of HMT. Due to the decreasing H_2CO abundance that we observe at doses higher than 10 eV/16u, a lower quantity of H_2CO would be available in the ice to form HMT during the subsequent warm-up, explaining why the dose affects the final amount of HMT in residues, as reported by Urso et al. (2020b). By warming up the frozen mixtures with a constant heating rate of 3 K min^{-1}, as reported in the literature for similar experiments (e.g. Urso et al. 2020b), after their irradiation up to doses well above this 10 eV/16u value, we do not detect any feature that would be attributable to HMT in the IR spectra. We thus expect astrophysical ices exposed to doses well above the threshold value of 10 eV/16u to be depleted in H_2CO and thus they would be less likely to lead to the formation of HMT in space.

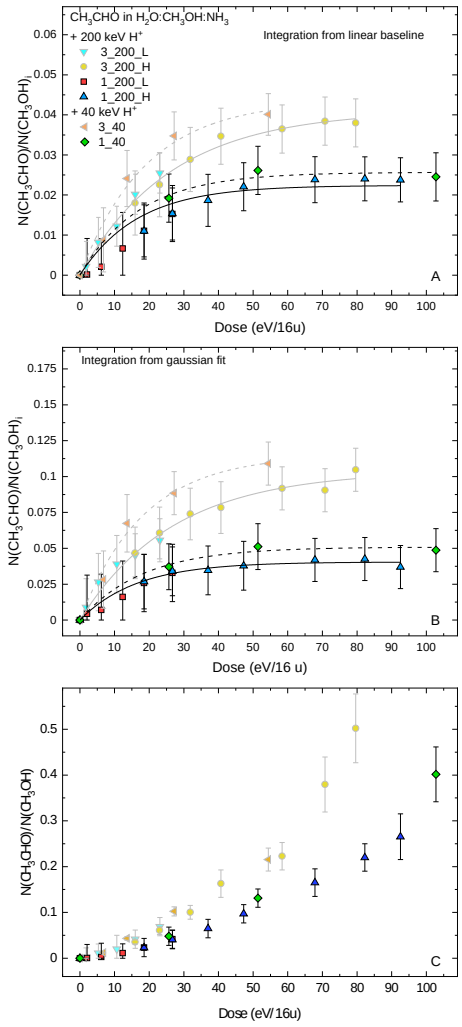

Fig. 6. CH_3CHO column density with respect to the initial methanol abundance ($(CH_3OH)i$, *panels A and B*) or during irradiation (CH_3OH, panel C). Estimates are based on the analysis of the 1350 cm^{-1} band for CH_3CHO and on the 1025 cm^{-1} band for CH_3OH. *Panel A*: estimates obtained after the subtraction of a linear baseline between 1360 and 1330 cm^{-1} and integration of the 1350 cm^{-1} band intensity. *Panel B*: estimates obtained from the integration of Gaussian curves centred at about 1350 cm^{-1} obtained after a multi-Gaussian fit performed in the range 1500–1300 cm^{-1}. *Panel C*: CH_3CHO with respect to the amount of CH_3OH during irradiation. The ratio is calculated using the abundances of CH_3CHO obtained with the method of the integration from linear baseline.

4.2. Astrophysical implications and timescales of irradiation in space

In this section, we estimate the timescales necessary to form H_2CO and CH_3CHO in ices exposed to energetic H^+ on icy grain mantles and on frozen surfaces in the outer Solar System.

To obtain the timescale of irradiation on icy grain mantles, we followed the estimations reported by Kaňuchová et al. (2016) and the approximation for the energy of cosmic ions reported by Mennella et al. (2003). Timescales of irradiation in dense molecular clouds, protostars, and protoplanetary disks can be evaluated from the measured cosmic-ray ionization rate ζ (s^{-1}). For our calculation, we considered the lowest and highest values of ζ estimated in different sources in the ISM reported by Mennella et al. (2003), Podio et al. (2014), Woods et al. (2015) and Kaňuchová et al. (2016). These values vary between

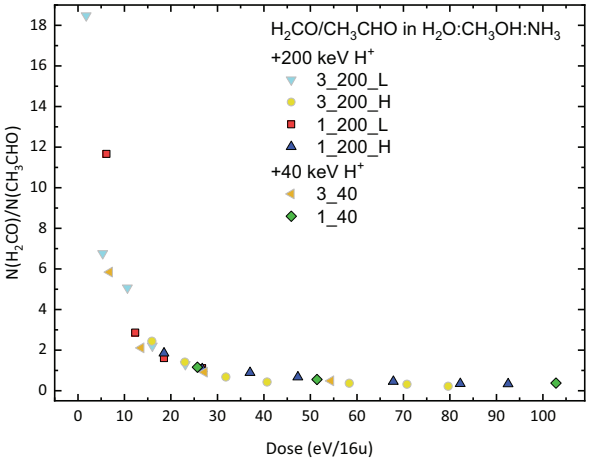

Fig. 7. H_2CO over CH_3CHO with respect to dose in H_2O:CH_3OH:NH_3 mixtures. Estimates are based on the analysis of the H_2CO 1250 cm^{-1} and of the CH_3CHO 1350 cm^{-1} bands.

1.3×10^{-15} s^{-1} and 1.3×10^{-17} s^{-1}. With this ζ, icy grain mantles would accumulate 10 eV/16u within 1.1×10^6 and 1.1×10^8 yr, respectively. At this dose, we find the highest abundance of H_2CO (Fig. 5), while the CH_3OH abundance decreases to about 40% of its initial value. Higher doses determine the destruction of H_2CO and at 60 eV/16u its abundance drops to 1% with respect to CH_3OH. Considering our most conservative estimates, up to 4% of CH_3CHO relative to the initial CH_3OH can form within ices exposed to irradiation. This abundance is reached at about 50 eV/16u, which corresponds to 5.5×10^6–5.5×10^8 yr. These timescales are comparable to the expected lifetimes of icy mantles in dense molecular clouds and in protoplanetary disks (e.g. Greenberg 1982; Larson 2003). However, when we take the data in Fig. 5 into account, the column density of H_2CO detected in icy grain mantles (e.g. Boogert et al. 2015) is higher than the amount that can form after CR irradiation of CH_3OH-rich ices, suggesting that other processes contribute to the formation of solid H_2CO in icy grain mantles, such as hydrogenation of solid CO (e.g. Watanabe & Kouchi 2002). So far, CH_3CHO is only tentatively detected in the line of sight of the high-mass YSO W33A (Schutte et al. 1999). In the near future, this tentative detection could be confirmed by *James Webb* Space Telescope (JWST) observations that may also include information on the CH_3CHO relative abundances and in turn contribute to constrain its formation route (e.g. McClure et al. 2017).

During the star-formation process, icy mantles sublimate and thus inject volatile species into the gas phase (e.g. Caselli & Ceccarelli 2012). Before sublimation, frozen species can react and form new compounds, however. In particular, the reaction between H_2CO and NH_3 is the first step of a more complex reaction leading to HMT (e.g. Bernstein et al. 1995; Vinogradoff et al. 2012b). The IR spectrum of HMT shows two intense and narrow bands at 1007 and 1234 cm^{-1} (Bernstein et al. 1994). Although the detection of the 1005 band would be hindered by the silicate feature at the same wavelength, the 1234 cm^{-1} band might be detected. However, even if the temperature would increase enough to allow the HMT formation, we estimate that the 1234 cm^{-1} HMT band would show an optical depth peak of about 2×10^{-2}–4×10^{-3} if we were to assume that 10–40% of NH_3 observed in interstellar ices would react to form HMT and if we used the spectral parameters reported by Bernstein et al. (1994, 1995). This value is below the detection limits of the instruments on board the JWST

(Wells et al. 2015). However, the presence of HMT in the early Solar System and its incorporation in the meteoritic parent bodies could explain the presence of such compounds in carbonaceous chondrites, although also hydrothermal aqueous alteration in asteroids may contribute to the formation of HMT Oba et al. (2020).

Since their formation, frozen bodies in the outer Solar System are exposed to SEP and to CR, although the shielding of the heliosphere strongly limits the flux of CR with energies lower than a few hundred MeV (e.g. Langner et al. 2003). CH_3OH is detected on 5145 Pholus (semimajor axis, S.A. 20.36 au), 2002 VE95 (S.A. 39.18 au), and 486958 Arrokoth (S.A. 44.58 au), but neither solid-phase H_2CO nor CH_3CHO are detected on frozen surfaces in the Solar System. By scaling the values reported by Strazzulla et al. (2003), who estimated the timescales of irradiation at various locations in the outer Solar System, we find that a frozen body located at 40 au accumulated about 65 eV/16u at surface depth of 1 μm and about 46 eV/16u at surface depth of 1 cm since its formation 4.6 billion years ago. Deeper layers, however, experience decreasing dose values.

The missing detection of HMT in CH_3OH-rich bodies could be explained by the fact that IR photons only probe limited thicknesses of the surface and HMT would only form in deeper layers, where the lower dose allows its precursors to form and survive. In the outer Solar System, we estimate that energetic ions can induce the formation of the highest abundance of H_2CO and CH_3CHO on timescales of about 10^6 yr (Urso et al. 2020b). These timescales imply a fast and efficient conversion of CH_3OH into its byproducts, including CH_4 and aldehydes. However, bodies in the Kuiper belt are thought to have remained largely undisturbed since their formation (e.g. Grundy et al. 2020). During their lifetime, these bodies might have accumulated doses up to 40–70 eV/16u by CR and much higher doses at smaller surface depth by SEP. These doses would destroy not only the complex organic precursors, but also volatiles species that are observed on frozen surfaces, however, including CH_3OH (e.g. Barucci et al. 2011). Nevertheless, our analysis on the irradiation of CH_3OH shows that its destruction reaches a plateau and that about 3% of CH_3OH survives at 100 eV/16u. Thus, lower quantities of CH_3OH could survive the high extent of irradiation on small bodies, and aldehydes could still form on highly irradiated surfaces. Another consideration regards the fact that IR photons that are detected by remote-sensing observations and that inform on the composition of frozen surfaces can probe larger thicknesses than the penetration depth of SEP (Urso et al. 2020a). Low-energy SEP alter a lower thickness than high-energy SEP and CR. IR photons might travel through both layers strongly altered by SEP and underlying layers that are only affected by CR and high-energy SEP. These buried layers, exposed to much lower doses, can still contain high quantities of CH_3OH and its irradiation byproducts, such as aldehydes, which might then take part in reactions to form complex organics. Furthermore, rejuvenating processes have to be taken into account as they cause the exposure of fresh and less altered materials buried below frozen surfaces. These unprocessed ices would then undergo ion bombardment and form byproducts within the short timescales reported above.

Cometary comae also show H_2O, CH_3OH, NH_3, H_2CO, and CH_3CHO along with various other compounds (e.g. Bockelée-Morvan et al. 2000; le Roy et al. 2015, and references therein). Oort cloud comets are exposed to high fluxes of CR that induce the formation of organic refractory materials, and Strazzulla & Johnson (1991) estimated that organic refractory materials form in the upper 1–2 m of cometary surfaces within the age of the Solar System. Deeper layers are less strongly irradiated, but about 2 eV/16u can cumulate because radioactive elements decay within the nucleus (e.g. Draganic & Draganic 1984; Modica et al. 2012).

Observational studies showed that the abundance of complex molecules relative to water in cometary comae is comparable (with differences smaller than one order of magnitude) to the abundances observed towards YSOs, supporting the hypothesis that comets inherited ices from the presolar cloud or that cometary ices were processed in the same physical and chemical ways as interstellar ices (e.g. Bockelée-Morvan et al. 2019, and references therein). Various comets show an abundance of H_2CO that is comparable to that of CH_3OH (e.g. le Roy et al. 2015; Schuhmann et al. 2019). Thus, other processes might contribute to the presence of H_2CO in addition to its formation from the CH_3OH-rich ices irradiation. On the other hand, the abundance ratio CH_3CHO/CH_3OH ranges between 0.01 and 0.2, which means that CH_3CHO might form after cosmic ion irradiation of CH_3OH-rich ices. However, CH_3CHO has been detected only towards a limited number of comets (e.g. le Roy et al. 2015; Bockelée-Morvan et al. 2019). The capabilities of the JWST will enable future observations to contribute to better constrain the origin of complex molecules in comets as well as on other frozen bodies located in the outer Solar System.

5. Conclusions

We exposed H_2O, CH_3OH, and NH_3 to 40 and 200 keV H^+ to simulate the irradiation of frozen surfaces in both the ISM and in the Solar System. We followed the destruction of CH_3OH and the formation of its byproducts CH_4, H_2CO, and CH_3CHO. We find that the composition of ices depends on the irradiation dose and that the abundance of aldehydes is affected by the amount of water in mixtures. In all mixtures, the H_2CO abundance decreased at doses higher than 10 eV/16u, thus ices exposed to a higher dose would be depleted in such a compound. In turn, lower abundances of HMT might form in the refractory organic material that is produced after irradiation and warm-up of ices due to the role of H_2CO as a precursor of HMT.

Frozen volatile compounds such as CH_3OH, aldehydes, and complex organics might be buried below the surface that is probed by astronomical observations. Volatile compounds might survive below surfaces and the irradiation by CR would induce the partial destruction of methanol and the formation of its byproducts, including aldehydes, which might then take part in reactions to form more complex compounds.

Further data are needed to better constrain the fate of organics after their formation, to understand how radiation affects their chemical properties, and to determine whether they can survive the harsh conditions on atmosphere-less surfaces. In this regard, exposure platforms on board space facilities allow the exposure to the full solar spectrum as well as to higher fluxes of galactic CR and solar particles (e.g. Baratta et al. 2015, 2019; Cottin et al. 2017; Bryson et al. 2015). The Organics Exposure in Orbit (OREOcube; Elsaesser et al. 2014) and Exocube (Sgambati et al. 2020) facilities will allow exposing various organic compounds of relevance for astrobiology as pure and in contact with mineral surfaces and gaseous compounds, allowing us to simulate the physico-chemical conditions of various astrophysical scenarios. Both platforms will allow the in situ analysis by means of UV-Visible (OREOcube) or mid-IR (Exocube) spectroscopy, allowing to monitor the sample evolution during flight. At the end of the mission, samples will be brought back to Earth allowing their further characterization. Both experiments will thus

provide information about the survival of organics and about the possibility that complex molecules formed after the processing of solid-phase simple volatiles can be trapped in small bodies and delivered on planetary surfaces.

Acknowledgements. We thank the referee, Dr. V. Vinogradoff for the useful comments to improve the manuscript. AE and RGU acknowledges the Einstein Foundation Berlin (grant IPF-2018-469). INGMAR is a IAS-IJCLab facility funded by the French Programme National de Planétologie (PNP), Faculté des Sciences d'Orsay, Université Paris-Sud (Attractivité 2012), P2IO LabEx (ANR-10-LABX-0038) in the framework Investissements d'Avenir (ANR-11-IDEX-0003-01). MEP, GAB, and CS acknowledge the financial support by the Italian Ministero dell'Istruzione, Università e Ricerca through the grant Progetti Premiali – iALMA.

References

Allen, M., & Robinson, G. W. 1977, ApJ, 212, 396
Altwegg, K., Balsiger, H., Berthelier, J. J., et al. 2017, MNRAS, 469, S130
Altwegg, K., Balsiger, H., & Fuselier, S. A. 2019, ARA&A, 57, 113
Baratta, G. A., Chaput, D., Cottin, H., et al. 2015, Planet. Space Sci., 118, 211
Baratta, G. A., Accolla, M., Chaput, D., et al. 2019, Astrobiology, 19, 1018
Barucci, M. A., & Merlin, F. 2020, in The Trans-Neptunian Solar System, eds. D. Prialnik, M. A. Barucci, & L. Young (Amsterdam: Elsevier), 109
Barucci, M. A., Alvarez-Candal, A., Merlin, F., et al. 2011, Icarus, 214, 297
Bennett, C. J., Jamieson, C. S., Osamura, Y., & Kaiser, R. I. 2005, ApJ, 624, 1097
Bernstein, M. P., Sandford, S. A., Allamandola, L. J., & Chang, S. 1994, J. Phys. Chem., 98, 12206
Bernstein, M. P., Sandford, S. A., Allamandola, L. J., Chang, S., & Scharberg, M. A. 1995, ApJ, 454, 327
Bockelée-Morvan, D., Leyrat, C., Erard, S., et al. 2019, A&A, 630, A22
Bockelée-Morvan, D., Lis, D. C., Wink, J. E., et al. 2000, A&A, 353, 1101
Boogert, A. C. A., Gerakines, P. A., & Whittet, D. C. B. 2015, ARA&A, 53, 541
Bottinelli, S., Ceccarelli, C., Williams, J. P., & Lefloch, B. 2007, A&A, 463, 601
Bouilloud, M., Fray, N., Bénilan, Y., et al. 2015, MNRAS, 451, 2145
Brown, M. E., Schaller, E. L., & Fraser, W. C. 2011, ApJ, 739, L60
Brucato, J. R., Baratta, G. A., & Strazzulla, G. 2006, A&A, 455, 395
Brunetto, R., Barucci, M. A., Dotto, E., & Strazzulla, G. 2006, ApJ, 644, 646
Bryson, K. L., Salama, F., Elsaesser, A., et al. 2015, Int. J. Astrobiol., 14, 55
Busemann, H., Young, A. F., O'D. Alexander, C. M., et al. 2006, Science, 312, 727
Caselli, P., & Ceccarelli, C. 2012, A&ARv, 20, 56
Cazaux, S., Tielens, A. G. G. M., Ceccarelli, C., et al. 2003, ApJ, 593, L51
Chan, Q. H. S., Franchi, I. A., Zhao, X., et al. 2020, Meteor. Planet. Sci., 55, 1320
Chan, Q. H. S., Stephant, A., Franchi, I. A., et al. 2021, Sci. Rep., 11, 5125
Chauvin, N., Dayras, F., Le Du, D., & Meunier, R. 2004, Nucl. Instrum. Methods Phys. Res. A, 521, 149
Ciaravella, A., Muñoz Caro, G., Jiménez Escobar, A., et al. 2010, ApJ, 722, L45
Codella, C., Fontani, F., Ceccarelli, C., et al. 2015, MNRAS, 449, L11
Cottin, H., Szopa, C., & Moore, M. H. 2001, ApJ, 561, L139
Cottin, H., Kotler, J. M., Billi, D., et al. 2017, Space Sci. Rev., 209, 83
Crovisier, J., Bockelée-Morvan, D., Colom, P., et al. 2004, A&A, 418, 1141
Cruikshank, D. P., Roush, T. L., Bartholomew, M. J., et al. 1998, Icarus, 135, 389
Dalle Ore, C. M., Fulchignoni, M., Cruikshank, D. P., et al. 2011, A&A, 533, A98
Danger, G., Orthous-Daunay, F. R., de Marcellus, P., et al. 2013, Geochim. Cosmochim. Acta, 118, 184
Danger, G., Fresneau, A., Abou Mrad, N., et al. 2016, Geochim. Cosmochim. Acta, 189, 184
Dartois, E., Augé, B., Boduch, P., et al. 2015, A&A, 576, A125
de Marcellus, P., Fresneau, A., Brunetto, R., et al. 2017, MNRAS, 464, 114
Delsanti, A., Merlin, F., Guilbert-Lepoutre, A., et al. 2010, A&A, 520, A40
Dougherty, M. K., & Spilker, L. J. 2018, Rep. Prog. Phys., 81, 065901
Draganic, I. G., & Draganic, Z. D. 1984, Adv. Space Res., 4, 115
Duvernay, F., Dufauret, V., Danger, G., et al. 2010, A&A, 523, A79
Elsaesser, A., Quinn, R. C., Ehrenfreund, P., et al. 2014, Langmuir, 30, 13217
Fray, N., & Schmitt, B. 2009, Planet. Space Sci., 57, 2053
Fresneau, A., Abou Mrad, N., d'Hendecourt, L. L., et al. 2017, ApJ, 837, 168
Fulvio, D., Sivaraman, B., Baratta, G. A., Palumbo, M. E., & Mason, N. J. 2009, Spectrochim. Acta A Mol. Biomol. Spectros., 72, 1007
Greenberg, J. M. 1982, IAU Colloq., 61, 131
Grundy, W. M., Binzel, R. P., Buratti, B. J., et al. 2016, Science, 351, aad9189
Grundy, W. M., Bird, M., Britt, D., et al. 2020, Science, 367, eaay3705
Hudson, R. L., & Ferrante, R. F. 2020, MNRAS, 492, 283
Hulett, H. R., Wolman, Y., Miller, S. L., et al. 1971, Science, 174, 1038
Islam, F., Baratta, G. A., & Palumbo, M. E. 2014, A&A, 561, A73
Jaber, A. A., Ceccarelli, C., Kahane, C., & Caux, E. 2014, ApJ, 791, 29
Johnson, T. V. 2005, Space Sci. Rev., 116, 401
Kaňuchová, Z., Urso, R. G., Baratta, G. A., et al. 2016, A&A, 585, A155
Khare, B. N., Thompson, W. R., Chyba, C. F., Arakawa, E. T., & Sagan, C. 1989, Adv. Space Res., 9, 41
Langner, U. W., Potgieter, M. S., & Webber, W. R. 2003, J. Geophys. Res. Space Phys., 108, 8039
Larson, R. B. 2003, Rep. Prog. Phys., 66, 1651
Le Roy, L., Altwegg, K., Balsiger, H., et al. 2015, A&A, 583, A2
McClure, M., Bailey, J., Beck, T., et al. 2017, IceAge: Chemical Evolution of Ices during Star Formation, JWST Proposal ID 1309. Cycle 0 Early Release Science
Meinert, C., Myrgorodska, I., de Marcellus, P., et al. 2016, Science, 352, 208
Mennella, V., Baratta, G. A., Esposito, A., Ferini, G., & Pendleton, Y. J. 2003, ApJ, 587, 727
Mewaldt, R. A., Cohen, C. M. S., Mason, G. M., Haggerty, D. K., & Desai, M. I. 2007, Space Sci. Rev., 130, 323
Mispelaer, F., Theulé, P., Aouididi, H., et al. 2013, A&A, 555, A13
Mitchell, D. L., Lin, R. P., Anderson, K. A., et al. 1987, Science, 237, 626
Modica, P., Palumbo, M. E., & Strazzulla, G. 2012, Planet. Space Sci., 73, 425
Moore, M. H., & Hudson, R. L. 1998, Icarus, 135, 518
Moore, M. H., Ferrante, R. F., & Nuth, J. A., I. 1996, Planet. Space Sci., 44, 927
Mulas, G., Baratta, G. A., Palumbo, M. E., & Strazzulla, G. 1998, A&A, 333, 1025
Nuevo, M., Auger, G., Blanot, D., & D'Hendecourt, L. 2008, Origins Life Evol. Biosph., 38, 37
Nuevo, M., Cooper, G., & Sandford, S. A. 2018, Nat. Commun., 9, 5276
Oba, Y., Takano, Y., Naraoka, H., et al. 2020, Nat. Commun., 11, 6243
Oba, Y., Takano, Y., Furukawa, Y., et al. 2022, Nat. Commun., 13, 2008
Öberg, K. I., Bottinelli, S., Jørgensen, J. K., & van Dishoeck, E. F. 2010, ApJ, 716, 825
Palumbo, M. E. 2006, A&A, 453, 903
Palumbo, M. E., Geballe, T. R., & Tielens, A. G. G. M. 1997, ApJ, 479, 839
Palumbo, M. E., Castorina, A. C., & Strazzulla, G. 1999, A&A, 342, 551
Parker, E. T., Chan, Q. H. S., Glavin, D. P., & Dworkin, J. P. 2022, Meteor. Planet. Sci., 57, 776
Pilorget, C., Okada, T., Hamm, V., et al. 2021, Nat. Astron., 6, 221
Podio, L., Lefloch, B., Ceccarelli, C., Codella, C., & Bachiller, R. 2014, A&A, 565, A64
Poston, M. J., Mahjoub, A., Ehlmann, B. L., et al. 2018, ApJ, 856, 124
Raunier, S., Chiavassa, T., Duvernay, F., et al. 2004, A&A, 416, 165
Rothard, H., Domaracka, A., Boduch, P., et al. 2017, J. Phys. B, 50, 062011
Schmitt-Kopplin, P., Gabelica, Z., Gougeon, R. D., et al. 2010, Proc. Natl. Acad. Sci., 107, 2763
Schuhmann, M., Altwegg, K., Balsiger, H., et al. 2019, ACS Earth Space Chem., 3, 1854
Schutte, W. A., Boogert, A. C. A., Tielens, A. G. G. M., et al. 1999, A&A, 343, 966
Sephton, M. A. 2002, Natural Product Rep., 19, 292
Sgambati, A., Deiml, M., Stettner, A., et al. 2020, Acta Astron., 166, 377
Spencer, J. R., & Nimmo, F. 2013, Ann. Rev. Earth Planet. Sci., 41, 693
Strazzulla, G., & Johnson, R. E. 1991, Irradiation Effects on Comets and Cometary Debris, Comets in the Post-Halley Era (Dordrecht: Springer Netherlands)
Strazzulla, G., Pirronello, V., & Foti, G. 1983, A&A, 123, 93
Strazzulla, G., Cooper, J. F., Christian, E. R., & Johnson, R. E. 2003, Comptes Rendus Phys., 4, 791
Theulé, P., Duvernay, F., Danger, G., et al. 2013, Adv. Space Res., 52, 1567
Urso, R. G., Scirè, C., Baratta, G. A., Compagnini, G., & Palumbo, M. E. 2016, A&A, 594, A80
Urso, R. G., Palumbo, M. E., Ceccarelli, C., et al. 2019, A&A, 628, A72
Urso, R. G., Baklouti, D., Djouadi, Z., Pinilla-Alonso, N., & Brunetto, R. 2020a, ApJ, 894, L3
Urso, R. G., Vuitton, V., Danger, G., et al. 2020b, A&A, 644, A115
Vinogradoff, V., Duvernay, F., Danger, G., Theulé, P., & Chiavassa, T. 2011, A&A, 530, A128
Vinogradoff, V., Duvernay, F., Farabet, M., et al. 2012a, J. Phys. Chem. A, 116, 2225
Vinogradoff, V., Rimola, A., Duvernay, F., et al. 2012b, Phys. Chem. Chem. Phys. Incorporating Faraday Transac., 14, 12309
Vinogradoff, V., Fray, N., Duvernay, F., et al. 2013, A&A, 551, A128
Watanabe, N., & Kouchi, A. 2002, ApJ, 571, L173
Wells, M., Pel, J. W., Glasse, A., et al. 2015, PASP, 127, 646
Woods, P., Occhiogrosso, A., Viti, S., et al. 2015, MNRAS, 450, 1256
Ziegler, J. F., Biersack, J. P., & Ziegler, M. D. 2008, The Stopping and Range of Ions in Solids (New York: Pergamon Press)

Appendix A: H^+ stopping power

Figure B.1 shows the simulations we ran with SRIM to estimate the stopping power, that is, the energy released by the impinging ion per unit path length, of 40 and 200 keV H^+ impinging on H_2O:CH_3OH:NH_3 mixtures. H^+ release their energy via inelastic collisions with the electronic cloud of the target molecules (electronic stopping power, S_e), while the energy released by elastic collisions with the nuclei of the target molecules (nuclear stopping power, S_n) is negligible.

Appendix B: Estimates of the 1350 cm^{-1} band

We here give an example of the two methods we used to estimate the 1350 cm^{-1} band area in the spectra of H_2O:CH_3OH:NH_3 mixtures after irradiation with 40 or 200 keV H^+. Panel A shows the estimate of the 1350 cm^{-1} band area after the subtraction of a linear continuum between about 1360 and 1330 cm^{-1}. Panel B shows the multi-Gaussian fit we used to model the same spectrum as reported in panel A. The dotted red line shows the modelled spectrum. In both panels, the grey area represents the integrated optical depth of the 1350 cm^{-1} band taken into account for our estimates.

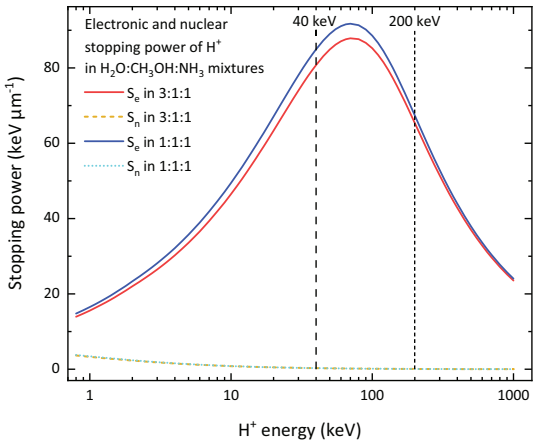

Fig. B.1. Elastic and nuclear stopping power (Bragg curves) of protons in H_2O:CH_3OH:NH_3=3:1:1 and 1:1:1 frozen mixtures as calculated by means of the SRIM software (Ziegler et al. 2008). The S_n curves overlap and cannot be distinguished on the given scale.

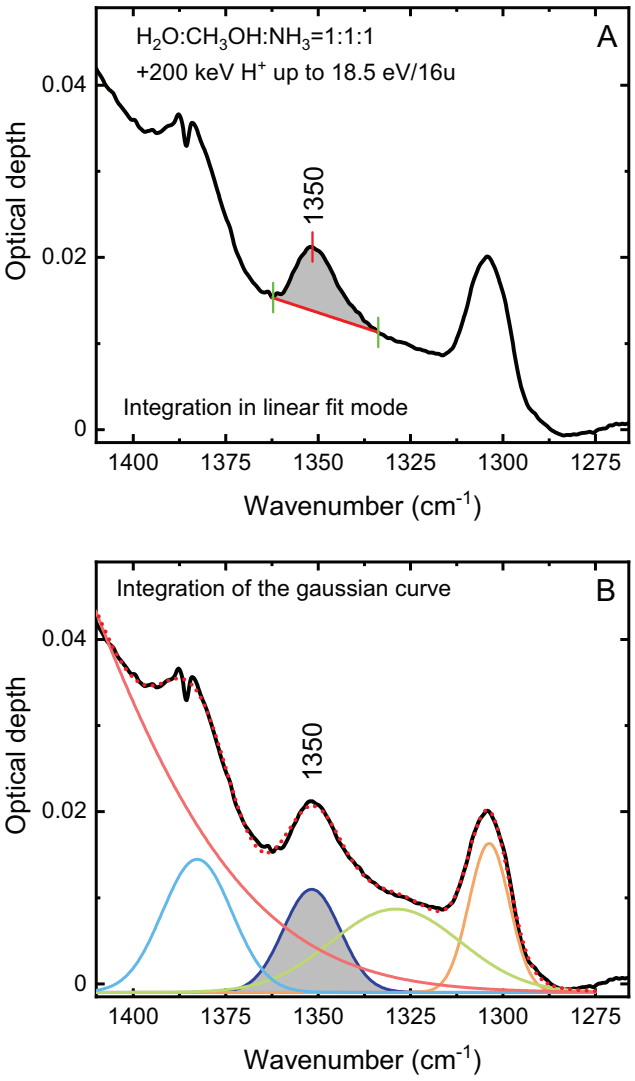

Fig. B.2. Estimates of the 1350 cm^{-1} band area in a H_2O:CH_3OH:NH_3=1:1:1 mixture bombarded with 200 keV H^+. Panel A: Integration of the optical depth after the subtraction of a linear continuum between about 1360 and 1330 cm^{-1}; Panel B: Multi-Gaussian fit between 1450-1250 cm^{-1} and estimate of the 1350 cm^{-1} band area from the integration of the optical depth of the synthetic Gaussian curve.